In situ x-ray-diffraction and -reflectivity studies of the Au(111)/electrolyte interface: Reconstruction and anion adsorption

Jia Wang and B. M. Ocko
Department of Physics, Brookhaven National Laboratory, Upton, New York 11973

Alison J. Davenport and Hugh S. Isaacs
Department of Applied Science, Brookhaven National Laboratory, Upton, New York 11973
(Received 29 August 1991; revised manuscript received 12 March 1992)

In situ x-ray-scattering studies of the Au(111) electrode surface have been carried out in NaF, NaCl, LiCl, CsCl, KCl, and NaBr solutions using grazing-incident-angle diffraction and reflectivity techniques. The top layer of gold atoms undergoes a reversible phase transition between the (1×1) bulk termination and a $(p\times\sqrt{3})$ uniaxial discommensuration (striped) phase on changing the electrode potential. Below the critical potential, in all solutions, $p=23$, which is identical to that obtained in vacuum. An ordered array of discommensuration kinks is not observed. Above the critical potential, $23<p<30$. At sufficiently positive potentials, the surface forms an ideally terminated (111) surface. In the negative potential sweep, the reconstruction starts to reform at the critical potential. Analysis of the potential dependence of the scattered x-ray intensity with differing anions in NaF, NaCl, and NaBr solutions supports a unifying model that depends on the induced surface charge density. The transition to the (1×1) phase is much faster than the formation of the reconstructed phase. Cycling the potential in the reconstructed region improves the reconstructed surface order. The adsorption of anions and "surface water" at the gold interface has been investigated using specular x-ray reflectivity.

I. INTRODUCTION

In vacuum, the three lowest-index faces of gold, (001), (110), and (111), have been the focus of scientific investigations over the past 25 years. At room temperature, these surfaces are reconstructed so that gold surface atoms are arranged in an ordered pattern with a periodicity and symmetry different from the underlying bulk layers.[1-13] Under electrochemical conditions, the surface charge can be varied continuously and reversibly by as much as 0.5 electrons per surface atom, yet very little is known about the atomic structure of electrified interfaces. Recent technical developments have permitted electrochemical surfaces to be investigated with an increasing level of sophistication. These developments, which include scanning tunneling microscopy (STM),[14-18] atomic-force microscopy,[19] and surface x-ray scattering,[20-22] have permitted electrochemical surfaces to be investigated on an atomic scale. In this paper we report the results of a comprehensive x-ray-scattering study of the $(23\times\sqrt{3})$ reconstruction of the Au(111) electrode surface in a number of different solutions. Some of these results have been previously reported.[23,24]

The possibility that electrochemically induced reconstructions of gold surfaces might exist was proposed by Hamelin on the basis of the hysteresis observed in differential capacitance curves and a peak that emerged in cyclic voltammograms (current-voltage curves) at the same potential.[25,26] *Ex situ* low-energy-electron-diffraction (LEED) studies have shown that the Au(111) surface, albeit after emersion from an electrochemical cell, forms a $(23\times\sqrt{3})$ phase in the negative potential regime.[2] *In situ* second harmonic generation (SHG) measurements at the Au(111) surface[27,28] have demonstrated that the phase transition between the $(23\times\sqrt{3})$ and (1×1) phases can be monitored by the additional symmetry pattern in the SHG intensity associated with the uniaxial compressed phase. However, it is difficult to extract detailed structural information from these measurements. Concurrent with the present surface x-ray-scattering study, *in situ* STM studies[29,30] in $HClO_4$ solutions have confirmed the existence of the $(23\times\sqrt{3})$ reconstruction within the negative potential regime. In the present electrochemical x-ray-scattering study, the characteristic stripe separation—averaged over a macroscopic area—versus the applied potential has been measured with a lateral resolution that exceeds the capability of current STM measurements.

Our understanding of the Au(111) surface in vacuum has been obtained from a variety of techniques including LEED,[3,4] transmission electron diffraction (TED),[5] helium scattering,[6] surface x-ray diffraction,[7,8] and STM.[31,32] The observed diffraction peaks have been interpreted in terms of a rectangular $(23\times\sqrt{3})$ unit cell that corresponds to a uniaxial compression of 4.4% as shown in Fig. 1. This structure is often referred to as a striped phase. From TED measurements,[5] helium scattering,[6] and from x-ray-diffraction techniques[8] it has been inferred that the surface atoms are arranged in a manner such that the surface stacking sequence changes between *ABC* and *ABA* as shown in Fig. 1. Recent x-ray-scattering[7,8] and STM studies[31,32] have shown that the uniaxial discommensuration direction rotates by $\pm60°$ to form a regular array of kink dislocations.

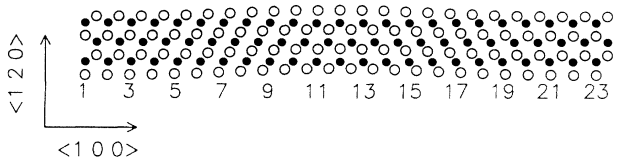

FIG. 1. In-plane hexagonal structure of the Au(111) surface. The solid circles correspond to atoms in the second top layer. Surface atoms (open circles) in the left- and right-hand sides of the figure are in undistorted hexagonal sites (*ABC* stacking sequence), whereas in the center of the figure the atoms are in faulted sites (*ABA* stacking sequence) (Refs. 6 and 7). For 24 surface atoms in place of 23 underlying surface atoms along the $\langle 100 \rangle$ direction, the compression is $24/23-1=4.4\%$ and $\delta=(\sqrt{3}/2)/23=0.038$.

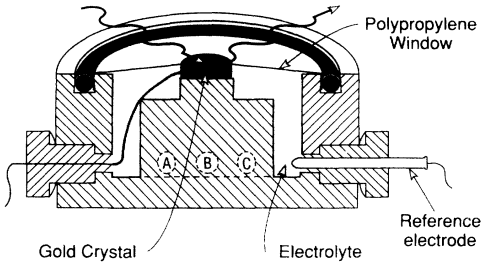

FIG. 2. X-ray-scattering electrochemical cell. The Au(111) single crystal is held at the top center by a Kel-F clamp. The cell is sealed with a polypropylene window compressed against the Kel-F cell by an o-ring. (a) Electrolyte input; (b) counter electrode; (c) electrolyte output. An outer chamber (not shown) is filled with nitrogen gas to prevent diffusion of oxygen through the polypropylene window.

In the present study we have characterized the potential dependence of the in-plane structure of the Au(111) surface in NaF, LiCl, NaCl, KCl, CsCl, and NaBr electrolytes with concentrations from 0.01 to 0.1 M (moles/liter). We have utilized salt solutions instead of the more commonly used acid solutions. Under these conditions we obtain a wider double-layer potential range and are able to determine whether cations have any effect on the structure of the Au(111) surface. In all the solutions, at sufficiently negative potentials, the surface forms a $(23\times\sqrt{3})$ structure as in vacuum. The surface diffraction pattern is inconsistent with a regular array of kink dislocations. At sufficiently positive potentials the striped reconstruction vanishes and the diffraction pattern exhibits the symmetry of the underlying lattice. The phase transitions are reversible in all solutions, although there are significant hysteresis effects.

In Sec. II we describe the details of the experiment. The results are reported in Sec. III with four subsections. X-ray-scattering measurements of the reconstructed phase and the general features of the potential-induced phase transition are presented in Sec. III A. In Sec. III B, the effects of different anions on the phase transition are reported and discussed in terms of the surface charge density $\sigma(E)$. Section III C describes the kinetic measurements of the phase transition upon a step change in the applied potential. In the Sec. III D, x-ray-reflectivity measurements of the Au(111)/electrolyte interfaces, both specular and nonspecular, are reported. Finally, we summarize our results in Sec. IV.

II. EXPERIMENT

A. Surface preparation and electrochemical conditions

Gold-disk electrodes (10 mm diameter by 2 mm thick) were spark cut from a common single crystal, and aligned along the nominal [111] direction. These disks were aligned, sanded, and polished with the [111] planes oriented within 0.1° of the surface-normal axis $\hat{n}$. A mirror finish was obtained using 1-μm alumina powder as the final mechanical polish. This was followed by electrochemical polish in a 1:1:1 (volume) HCl:ethylene glycol:ethanol solution.[33] The final surface preparation step involved sputtering with argon at 5×10^{-5} torr at 800 °C using a defocused beam at 1 kV and 2 μA for several hours. The sample was transferred through air to an electrochemical x-ray-scattering cell constructed from Kel-F (Ref. 20) as shown in Fig. 2.

A 6-μm polypropylene window sealed the cell with a thin-capillary electrolyte film between the crystal face and the polypropylene film. An outer chamber was flushed with N_2 gas to prevent oxygen from diffusing through the polypropylene membrane. The applied potential was referenced to a Ag/AgCl (3-M KCl) electrode connected to the cell through a microglass frit.[34] In order to reduce further the possibility of chloride contamination from the reference electrode, a second frit was added and the path separating the two frits was filled with NaF electrolyte. Counter electrodes were either gold or platinum wires.

Before use, the x-ray-scattering cell was cleaned with the 1:3 mixture of H_2O_2 (30%) and H_2SO_4 (98%) in order to minimize organic contaminants, followed by several rinsing and soaking cycles with Millipore water[35] to remove adsorbed SO_4^{2-} ions. The electrolyte solutions were prepared from superpure NaF, LiCl, NaCl, KCl, CsCl, and NaBr (Ref. 36) with Millipore H_2O. The NaF salts were baked for 2 h at 700 °C to remove trace amounts of volatile impurities. The diluted electrolyte solutions were deoxygenated with 99.999% N_2 gas[37] immediately before filling the cell. After flushing the cell with N_2 gas, the deoxygenated electrolyte was injected into the cell through a syringe. The cell was filled with enough solution to expand the polypropylene window, leaving a thick electrolyte layer (several mm) between the face and the window. The potential control was then turned on and cyclic voltammograms were carried out in this geometry to check the electrochemical conditions. Before carrying out the x-ray-scattering measurements, the cell was deflated leaving a thin electrolyte layer which we estimate from the small angle reflectivity measure-

ments to be between 10 and 20 μm thick. In the thin-electrolyte-layer geometry, the effects of bulk impurities are greatly reduced relative to the thick-electrolyte-layer geometry.

Our studies of the Au(111) surface were carried out in a potential range which is referred to as the "double-layer" region. Within this potential range there are no Faradaic processes and the electrode can be treated as an ideally polarizable interface. The potential region in which this approximation is valid is bounded by hydrogen evolution at negative potentials and gold oxidation processes at positive potentials. In salt solutions (pH about 6), hydrogen evolution occurs below -0.8 V. The high potential limit was 0.8 V for F^- and Cl^--containing solutions and 0.6 V for NaBr solutions.

B. X-ray scattering and reflectivity

The x-ray-scattering measurements were carried out with focused, monochromatic synchrotron radiation at beam lines X22B, X22C, and X25 at the National Synchrotron Light Source at Brookhaven National Laboratory. In the four-circle geometry, the sample was oriented through its Euler angles θ, χ, and ϕ (Ref. 38) by a spectrometer under computer control. The magnitude of the scattering wave vector is

$$|\mathbf{k}_f-\mathbf{k}_i|=4\pi/\lambda\sin(2\theta/2)\ ,$$

where $\mathbf{k}_i$ and $\mathbf{k}_f$ correspond to the incident and scattered wave vectors and where 2θ is the detector angle within the scattering plane. Diffraction measurements were carried out by measuring the scattering intensity along paths in reciprocal space.

Measurements were carried out at energies corresponding to wavelengths $\lambda=1.54$ Å (beam line X22B) and $\lambda=1.24$ Å (beam line X22C). For both these bending-magnet beam lines the focused flux (0.5×0.5 mm^2) was approximately 10^{11} photons. X-ray-scattering studies of the reconstruction kinetics were also performed at $\lambda=1.18$ Å at the X25 wiggler line. This beam line provides significantly greater flux than the bending-magnet lines. The scattered intensity at all three beam lines was measured with a scintillator detector placed on the 2θ arm and was normalized to the incident flux. At grazing incidence, i.e., small α, the incident x rays illuminate a region of the crystal 0.5 mm wide across the entire crystal face (10 mm). The scattering resolution, in reciprocal space, was primarily determined by the angular acceptance of the scattered radiation and the mosaic of the Au(111) crystal. The illuminated area of the incident beam does not directly affect the resolution. For the present measurements, the resolution within the scattering plane was determined by an array of equally spaced parallel plates (Soller slits) which provide a 2θ resolution of 0.1° half width at half maximum (HWHM). This corresponds to a longitudinal in-plane resolution in reciprocal space of 0.007 Å^{-1} HWHM at $\lambda=1.54$ Å and 0.009 Å^{-1} HWHM at $\lambda=1.24$ and 1.18 Å. The transverse in-plane resolution was limited by the mosaic spread of the crystalline order, which is typically 0.025° HWHM. Normal to the scattering plane, the resolution was determined by 10-mm detector slits located on the four-circle 2θ arm about 600 mm from the sample position.

In order to describe the scattering wave vector in terms of its components in the surface plane and along $\hat{n}$, it is convenient to use a hexagonal coordinate system.[8,39,40] The reciprocal basis can be expressed as

$$\mathbf{B}_1=\frac{2\pi}{a_0}\left[\frac{-4}{3},\ \frac{2}{3},\ \frac{2}{3}\right]_{\text{cubic}}\ , \tag{1a}$$

$$\mathbf{B}_2=\frac{2\pi}{a_0}\left[\frac{-2}{3},\ \frac{-2}{3},\ \frac{4}{3}\right]_{\text{cubic}}\ , \tag{1b}$$

$$\mathbf{B}_3=\frac{2\pi}{a_0}\left[\frac{1}{3},\ \frac{1}{3},\ \frac{1}{3}\right]_{\text{cubic}}\ , \tag{1c}$$

where

$$a^*=|\mathbf{B}_1|=|\mathbf{B}_2|=\frac{4\pi}{a\sqrt{3}}=2.52\ \text{Å}^{-1}\ ,$$

$$c^*=|\mathbf{B}_3|=\frac{2\pi}{a_0\sqrt{3}}=0.89\ \text{Å}^{-1}\ ,$$

and $a_0=4.08$ Å. The nearest-neighbor separation a equals $a_0/\sqrt{2}=2.885$ Å. An arbitrary position in hexagonal reciprocal space is represented by (H,K,L) or (H,K) within the surface plane where

$$\mathbf{G}=H\mathbf{B}_1+K\mathbf{B}_2+L\mathbf{B}_3\ . \tag{2}$$

The relationship between the $(h,k,l)_{\text{cubic}}$ and (H,K,L) is given by the transformations

$$h=-4H/3-2K/3+L/3\ ,$$

$$k=2H/3-2K/3+L/3\ ,$$

and

$$l=2H/3+4K/3+L/3\ .$$

For example $(1,1,1)_{\text{cubic}}=(0,0,3)$, $(0,0,2)_{\text{cubic}}=(0,1,2)$, and $(0,2,2)_{\text{cubic}}=(1,0,4)$. A schematic view of reciprocal space is shown in Fig. 3. The open circles correspond to allowed Bragg reflections and the solids lines correspond to the rods of weak scattering, which are referred to in the literature as truncation rods[41] or reflectivity.[42]

An important aspect of the present x-ray-diffraction study is the relationship between the in-plane surface structure and the surface-normal structure. The surface-normal structure, versus the applied potential, has been investigated by utilizing x-ray specular reflectivity. In an x-ray-reflectivity study, the weak scattering between the Bragg reflections depends on the exact arrangement of the surface atoms along the surface-normal direction. A brief review of x-ray reflectivity follows.

In the kinematic approximation, the reflectivity is calculated by integrating the x-ray-scattering cross section.[8,20,41–43] For an incident polarization orthogonal to the scattering plane, the expression for the reflectivity is given by

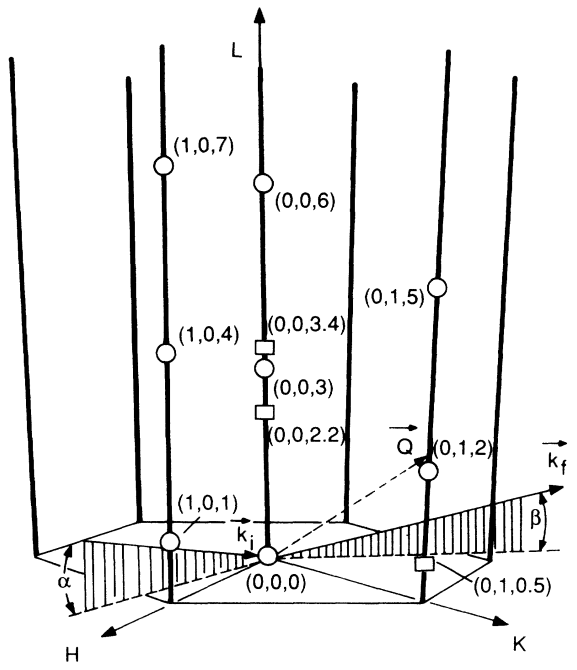

FIG. 3. Diffraction from the Au(111) surface in hexagonal reciprocal-space coordinates. The circles correspond to Bragg peaks and the lines are the rods of scattering connecting the Bragg peaks along the surface-normal direction. The squares correspond to positions where the potential dependence of the intensity is recorded in Figs. 7 and 16.

$$R(H,K,L)=|T(Q_z)|^4\left[\frac{256\pi^2 r_0}{3a^2Q_z^2}\right]\times|F_{\mathrm{Au}}(Q_z)e^{-W(Q_z)}S(H,K,L)|^2\ , \tag{3a}$$

where $W(Q_z)$ is the Debye-Waller factor,[42] $T(Q_z)$ is the Fresnel surface enhancement factor,[42] r_0 is the Thomson radius, and $Q_z=Lc^*$. The atomic form factor F_{Au} is approximately equal to the number of electrons in the gold atom at small wave vectors.

For a perfectly terminated Au(111) surface, the Fourier sum over atomic layers is nonzero when H and K are integers and is given by

$$S(H,K,L)=\sum_{n=1}^{\infty}e^{2\pi ni/3(-H+K+L)}\ . \tag{3b}$$

For noninteger H and K the sum goes to zero. Carrying out the geometric sum over the atomic layers gives the relationship

$$|S(H,K,L)|=\frac{1}{2\sin[\pi/3(-H+K+L)]}\ . \tag{3c}$$

When the denominator in Eq. (3c) equals zero, the scattering from all the atomic layers adds coherently. This corresponds to three-dimensional Bragg scattering. In addition, Eq. (3c) gives rise to weak scattering connecting the Bragg reflections. The scattering near a Bragg peak at (H,K,L_0) falls off sharply along L and can be approximated by $(L-L_0)^{-2}$. Specular reflectivity corresponds to the case where $H=K=0$, which yields Bragg peaks at $L=3j$, where j is an integer, and weak scattering between the Bragg peaks given by Eq. (3). For a perfectly terminated surface, $|S(H,K,L)|$ reaches a minimum exactly in the middle of the zone between two adjacent Bragg peaks along L. At this position the magnitude of $S(H,K,L)$ corresponds to the equivalent scattering from half of a gold monolayer. For reconstructed or otherwise nonideally terminated surfaces, the scattering amplitudes from each atomic layer close to the surface are no longer equivalent to those in the bulk. Therefore, changes in the surface-normal structure can be monitored by measuring specular intensities at fixed positions in reciprocal space. We demonstrate, in Sec. III D, that adsorbate species also modify the specular reflectivity profiles.

III. RESULTS AND DISCUSSION

A. The $(p\times\sqrt{3})$ reconstruction and potential-induced phase transition

An important feature of the Au(111) surface reconstruction is a uniaxial compression of the top layer of gold atoms, which forms a $(p\times\sqrt{3})$ rectangular unit cell as shown in Fig. 1. In a surface-diffraction measurement, the $(p\times\sqrt{3})$ reconstruction gives rise to additional in-plane reflections beyond the underlying (1×1) reflections. As previously demonstrated,[3–8] the reconstruction reflections are arranged in a hexagonal pattern surrounding the integer (H,K) positions. The incommensurability δ equals $(\sqrt{3}/2)/p$ (the bottom panel of Fig. 4). For example, if there are 24 surface atoms in place of 23 underlying surface atoms, the compression is $24/23-1=4.4\%$ and $\delta=(\sqrt{3}/2)/23=0.038$. In an x-ray-scattering experiment, the intensity is collected over several mm^2. Therefore, all three symmetry-equivalent domains, which are labeled by the three different open symbols in Fig. 4, are probed.

In the bottom panel of Fig. 4, equal-intensity contours are shown in the vicinity of the (0,1) reflection at $L=0.5$ for 0.01-M NaCl at -0.3 V. Four peaks surrounding the (0,1) reflection are arranged in a hexagonal pattern, where $\delta=0.038$ is the distance between (0,1) and the hexagonal vertices which corresponds to $p=\sqrt{3}/(2\delta)=23$. Our electrochemical measurements of the incommensurability are in good agreement with high-resolution vacuum measurements at $T=300$ K, where $\delta=0.0383$.[3–8] The two surface reflections at the largest wave-vector transfer from the origin are the most intense. The two reflections with the smallest wave-vector transfer correspond to higher-order modulation peaks and are not observed.[7,8] At sufficiently positive applied potentials, in all electrolytes, the scattering from the Au(111) surface does not exhibit the diffraction pattern of a reconstructured surface. Instead, only the integral reflections (H,K) originating from the substrate are observed.

We have carried out a study of the potential dependence of the scattering from the Au(111) surface through the (0,1) reflection along the [11] direction, which we label as the q_r axis in Fig. 4. Along the q_r (dimensionality

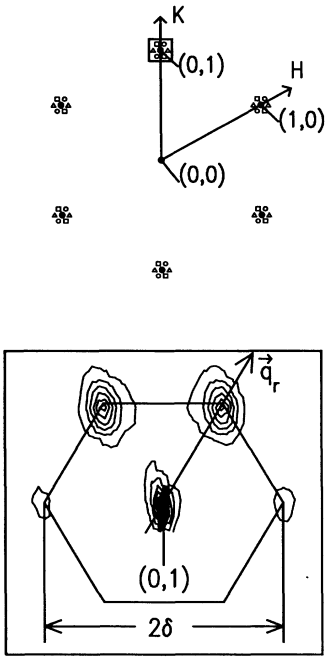

FIG. 4. Top: In-plane diffraction pattern of the $(23\times\sqrt{3})$ reconstruction in hexagonal coordinates. The solid circles are at the periodicities from the underlying bulk substrate. The open symbols originate from the $(23\times\sqrt{3})$ reconstructed phase with three rotationally equivalent domains. The axis q_r is defined to be along the [11] direction. Bottom: X-ray-scattering equal-intensity contours in the vicinity of the (0,1) reflection at $L=0.5$ measured in 0.01-M NaCl at -0.3 V.

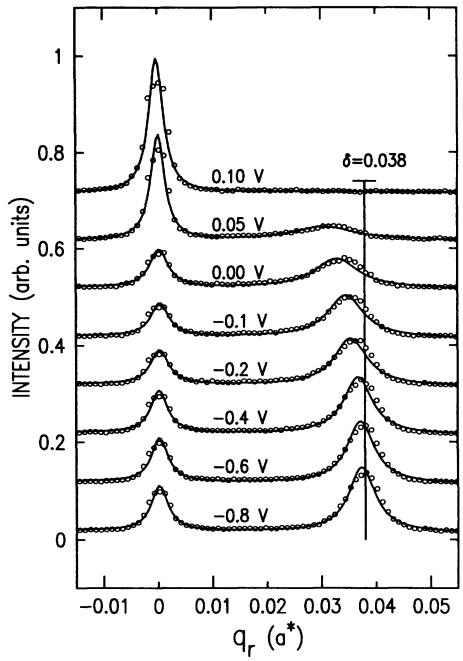

FIG. 5. Representative x-ray-scattering profiles along the q_r axis [see Fig. 4(b)] at $L=0.2$ in 0.01-M NaCl solution at a series of potentials chosen from scans between 0.1 and -0.8 V in steps of -0.05 V. The solid lines are fits to a Lorentzian line shape described in the text.

Å^{-1}) axis, the in-plane projection of the scattering-wave vector is give by $(q_r/\sqrt{3}a^*, 1+q_r/\sqrt{3}a^*)$. In Fig. 5, we present the measured scattering intensity obtained in 0.01-M NaCl along the q_r axis at $L=0.2$ at a series of decreasing potentials between 0.1 and -0.8 V with an effective scan rate of 0.5 mV/sec. Each data point was obtained by summing the scattered intensity for two sec at a constant potential. At 200-mA synchrotron ring current, the peak intensity at (0,1) can exceed 10^5 counts per second after background subtraction. Above 0.10 V the scattering is centered at $q_r=0$ (Fig. 5) corresponding to the (0,1) bulk reflection. As the potential is reduced below 0.05 V, the intensity of the reconstruction peaks grows. Concomitantly, the (0,1) reflection decreases in intensity. The position of the reconstruction peak moves outward (increasing compression) as the potential is decreased. The maximum scattering intensity at (0,1) is about 30 times the diffuse scattering originating from the electrolyte and window.

To extract additional information from the scattering profiles, we fitted the scattering profiles along q_r to the sum of two Lorentzians and a small background

$$S(q_r)=\frac{I_0}{1+(q_r/a^*)^2/\sigma^2}+\frac{I_\delta}{1+(q_r/a^*-\delta)^2/\sigma_\delta^2}+A+Bq_r/a^* . \quad (4)$$

The first term represents the scattering around (0,1), the second term corresponds to the scattering centered at $(\delta/\sqrt{3}, 1+\delta/\sqrt{3})$, and A and B are the background parameters. The parameters I_0 and I_δ correspond to the peak intensities at q_r equal to zero and δa^*, respectively. The Lorentzian profile widths in Eq. (4) are σ and σ_δ. In reciprocal space, the Lorentzian line shape is derived from a one-dimensional real-space atomic model in which the correlation function decays exponentially with a length $\zeta_\delta=a\sqrt{3}/(4\pi\sigma_\delta)$. This length is a measure of the distance over which atoms in the reconstructed layer are positionally correlated. The stripe separation L_δ is given by $L_\delta=pa=a\sqrt{3}/(2\delta)$.

In an x-ray-scattering measurement, the correlation length of the underlying Au(111) facets can also be determined from the inverse peak widths in reciprocal space. If the surface is composed of terraces (facets) separated from each other by monoatomic steps, the scattering from neighboring facets adds out of phase at the (0,1) reflection and the peak width is broadened by this effect. For an exponential facet size distribution, the mean facet size along the [11] direction, ζ, equals $a\sqrt{3}/(4\pi\sigma)$. In the present set of measurements, ζ is at least 300 Å and represents a lower bound for the distance between steps. Incorporating finite resolution effects into the analysis increases the effective facet size.

In the fitting procedure, the peak position δ, the widths σ and σ_δ, the amplitudes I_0 and I_δ, and the background are varied for the scattering profiles at constant potential. Instrumental resolution effects have not been included in

the present analysis since improving the reciprocal-space resolution by a factor of ten did not modify the observed scattering line widths.[44] The scattering in the wings of the peak at $q_r=0$ (substrate periodicity) exhibit a q_r^{-2} falloff. At small q_r, however, the scattering profiles are not adequately represented by the model. In part, this discrepancy is due to finite substrate mosaic effects, which have a Gaussian component that is not included in our Lorentzian model. At $q_r=0.038a^*$ (reconstructed periodicity) the scattering is reasonably well represented by the Lorentzian profiles at sufficiently negative potentials. The scattered intensity in the vicinity of $q_r=0.038a^*$ exhibit q_r^{-2} tails. However, the actual scattering is asymmetric, as shown in Fig. 5. This lineshape effect is most apparent when the potential undergoes a rapid potential excursion. The line shape is nearly a perfect Lorentzian if the potential is cycled within the reconstructed potential region. Consequently, we believe that this asymmetry results from the distribution of domains with a range of p.

The stripe separation L_δ and the correlation length ζ_δ obtained from fits to Eq. (4) are shown in Figs. 6(a) and 6(b), respectively as a function of the applied potential. The potential cycle originates at 0.1 V and continues to -0.8 V and then back to 0 V in steps of 0.05 V. After the initial signs of the surface reconstruction at 0.05 V, corresponding to the emergence of the modulation peak, there is a continued compression as the potential is decreased, as shown by the inverted triangles in Fig. 6(a). The maximum compression corresponds to a stripe separation of $23a$. Changes in the reconstructed surface structure virtually cease below -0.6 V. (In some cases, we have observed a small increase in p at the negative potentials. We do not understand the origin of this behavior.) Further compression and an increase in the correlation length resumes after changing the potential sweeping direction. The stripe domain correlation length ζ_δ achieves a maximum value of $55a$ at -0.1 V. This is at a potential just below where the reconstruction lifting starts and ζ_δ is always less than ζ. The correlation length can be increased by 10–30 % by cycling the potential between -0.8 and -0.1 V. The final state is reached after cycling the potential for several hours. We refer to the surface state where the maximum compression and correlation length are achieved as the "groomed" surface.[24]

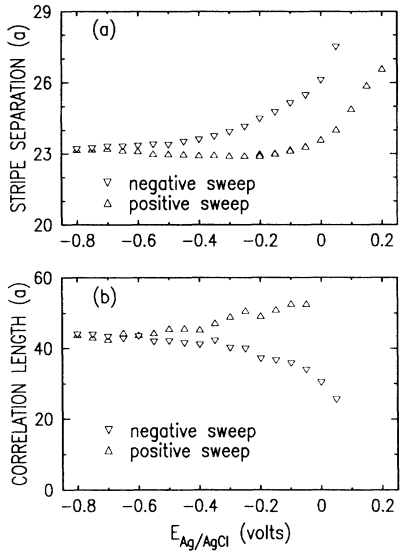

FIG. 6. (a) The stripe separation and (b) correlation length obtained by fitting the scattering profiles (as representatively shown in Fig. 5) to Eq. (4).

In vacuum, the surface forms an ordered array of 60° shifts in the discommensuration direction.[7,8,31,32] For the Si(111) surface, an ordered array of reconstructed domains with different orientations reduces the strain energy of the underlying substrate.[45] This argument may also apply to the Au(111) surface.[7,8] These shifts in the discommensuration direction (kinks) for the Au(111) surface are separated by about $80a$ at $T=300$ K. This wave vector, $\sim 2\pi/80a$, gives rise to additional diffraction spots.[7,8] At the electrode surface, at all potentials, these additional diffraction spots are absent. Hence, there is no evidence that the kinks form an ordered array. However, the Au(111) electrode surface may form a disordered array of kinks. This may explain why the maximum measured correlation length ($55a$) of the $(23\times\sqrt{3})$ reconstruction is smaller than the effective facet size.

In 0.01-M LiCl and CsCl there is no significant difference in the line shapes along q_r or in the potential dependence when compared with those in 0.01-M NaCl. Thus, the cation species has a minor effect on the Au(111) surface structure and potential dependence. As we shall see in the next section, changing the anion from Cl^- to F^- or Br^- ions has a marked effect on the potential dependence of the scattering. However, the in-plane surface structure in the groomed state appears virtually the same in all the salt solutions as well as in a $HClO_4$ solution. This observed leads to a quantitative procedure for comparing scattering intensities in different electrolyte solutions.

Complementary information on the Au(111) surface structure can be obtained by monitoring the potential dependence of the scattering at several positions along the rods of scattering (Fig. 3). Different positions in reciprocal space are sensitive to different aspects of the surface structure and likewise the potential dependence varies with reciprocal space position. For instance, scattering at (0,1) couples to the Fourier transform of the atomic density distribution within the surface plane at a wave vector corresponding to the undistorted bulk hexagonal spacing. The scattering at the reconstructed position increases with decreasing potential, whereas the scattering at (0,1,0.5) increases when the reconstruction is lifted at positive potentials. In contrast, the scattering along the specular direction is sensitive to changes in the density and interlayer expansion of the gold surface, as well as to adsorbed solution species.

Figure 7 displays the potential dependence of the scattering from the Au(111) surface in 0.01-M NaCl at (a) $(0.038/\sqrt{3},1+0.038/\sqrt{3},0.2)$, (b) (0,1,0.5), and (c) (0,0,3.4). Each panel corresponds to a potential cycle starting at 0.6 to -0.8 V and then back to 0.6 V at a sweep rate of 1.0 mV/sec. In the top panel [Fig. 7(a)] the scattering intensity corresponds to the principal

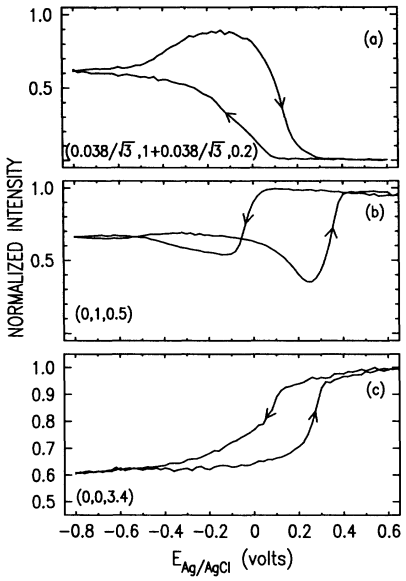

FIG. 7. Potential dependence of the x-ray-scattering intensities in 0.01-M NaCl solution at a scan rate of 1 mV/sec. Data were acquired at the reciprocal-space positions (a) $(0.038/\sqrt{3},1+0.038/\sqrt{3},0.2)$, (b) (0,1,0.5), and (c) (0,0,3.4) in both the negative and positive slew directions as indicated by the arrows. In all cases, the potential cycle starts at the positive limit. The background subtracted intensities are normalized to unity at their maximum values at all three positions.

$(23\times\sqrt{3})$ reconstruction peak. We have subtracted the diffuse background and normalized the intensity to the groomed state. At 0.05 V, the intensity at $(0.038/\sqrt{3},1+0.038/\sqrt{3},0.2)$ starts to increase corresponding to the formation of the reconstructed phase. Note that the maximum scattered density is achieved in the positive-going potential sweep before the reconstructed phase is lifted. The measured intensity at $(0.038/\sqrt{3},1+0.038/\sqrt{3},0.2)$ does not always reflect the peak intensity along q_r since δ varies with potential as shown in Fig. 5. Despite this fact, the potential dependence at this position does provide a reasonable measure of the reconstructed order parameter. This is because the peak profiles are relatively broad compared to the changes in δ with potential.

The scattering at (0,1,0.5) versus the applied potential is shown in Fig. 7(b), where the maximum scattering intensity has been normalized to unity. This reciprocal-space position is exactly halfway between the $(0,1,\bar{1})$ and (0,1,2) Bragg peaks. At this position, the measured intensities are most sensitive to effects of surface disorder. The decrease in the scattered intensity at (0,1,0.5) in the negative-going sweep occurs at 0.05 V which is the potential where the reconstruction starts to form [Fig. 7(a)]. This implies that the loss of order at (0,1) is correlated with the formation of the reconstructed phase. At the most negative potential (-0.8 V), the intensity at (0,1,0.5) falls to about 65% of the (1×1) value. In the positive sweep direction, the loss of the reconstructed order is nearly complete by 0.25 V, Fig. 7(a), whereas the (1×1) order as monitored at (0,1,0.5) is not completely restored until 0.40 V. A dip in the scattering intensity at (0,1,0.5) appears in Fig. 7(b) during both scan directions. In the positive sweep direction this effect is most pronounced and the intensity at 0.25 V falls to 35% of the intensity at 0.6 V. We believe that the dip in the scattering intensity corresponds to increased surface disorder during the phase-transition process.

The scattering along the specular direction, between neighboring Bragg peaks, provides information on the surface-normal structure and can be simply related to the sum over atomic layers with an appropriate density and phase factor.[42] The potential dependence of the scattered intensity along specular positions provides information on the phase behavior of the gold surface layers[20] as well as adsorbed anion species. In Fig. 7(c), the potential scan at (0,0,3.4) is shown. At this specular position, the scattered intensity is relatively insensitive to the effect of adsorbates. However, the intensity is very sensitive to the distance between the top two gold layers which decreases when the surface reconstructs. In this regard, the sharp intensity decrease (negative potential sweep) at 0.12 V results from the interlayer expansion of the top gold layer which precedes the development of a reconstructed phase at 0.08 V with in-plane order [Fig. 7(a)]. Between -0.5 and -0.8 V, in both sweep directions, there is very little change in the scattered intensity at (0,0,3.4). This is consistent with the idea that there is no significant change in the surface-normal structure within this potential range. In contrast, there is a continued increase in the scattered intensity at

$$(0.038/\sqrt{3},1+0.038/\sqrt{3},0.2)$$

within this same potential range. Thus, we conclude that the grooming process primarily involves a rearrangement of the gold atoms within the surface plane. In the lifting process, the sharp increase in slope at about 0.20 V indicates a decrease in the interlayer spacing of the top gold layer, which follows the loss of the in-plane order that starts at 0.00 V. This implies that there is an intermediate potential region in which the gold surface atoms have started to disorder within the plane but in which the surface-normal structure remains in the reconstructed state.

In order to explore the change of in-plane structure during the lifting within this intermediate potential range, we have carried out measurements of the scattering line shape in a 0.01-M solution of NaF. We have chosen the NaF electrolyte for this study since the phase transition occurs over the widest potential range. The surface was first groomed to form a well-ordered $(23\times\sqrt{3})$ reconstruction and scans were carried out along the q_r axis. The data were acquired in potential steps of 0.05 V. For each potential step, three scans were obtained in 10 min. The latter two scans were indistinguishable. In Fig. 8 (top) we show the last scan (of the three-scan sequence) along q_r at 0.0 V (triangles), 0.15 V (circles), and 0.25 V (squares). As the potential increases, the peak position δ decreases corresponding to an increased stripe separation. Furthermore, the width of the scattering profile increases with increasing potential. The

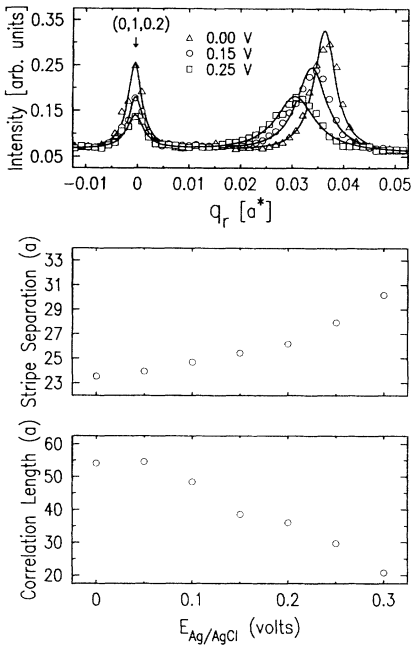

FIG. 8. Top: In-plane diffraction along q_r at 0.0 V (triangles), 0.15 V (circles), and 0.25 V (squares) in 0.01-M NaF. The solid lines are fits to Eq. (4) as described in the text. Stripe separation p (middle panel) and correlation length ζ_δ (bottom panel) are obtained from the fits as representatively shown in the top panel.

scattering profiles in Fig. 8 are well described by Lorentzian fits (solid lines) to Eq. (4). We have obtained the stripe separation L_δ and the correlation length ζ_δ from these fits which are shown in the bottom two panels of Fig. 8. The stripe separation increases from $23.5a$ at 0.0 V to $30.3a$ at 0.3 V. Correspondingly, the correlation length decreases from $55a$ to $20a$. In addition to the decrease of the correlation length, the intensity at the (0,1,0.2) position also decreases as shown in Fig. 8 (top panel). Thus, in the lifting process, there is an intermediate potential range between the $(23\times\sqrt{3})$ and the (1×1) phase in which the stripe separation is greater than $23a$ and in which the reconstructed surface is more disordered than in the $(23\times\sqrt{3})$ phase. At the most positive potentials, within this intermediate potential range, the interlayer expansion of the top gold layer starts to revert to the (1×1) state. Similar behavior is also observed in NaCl and NaBr solutions, although this effect occurs over a smaller potential range.

In this section the effects of potential on the Au(111) electrode in 0.01-M NaCl and NaF were presented in order to demonstrate the general features of the potential-induced phase transition. Analysis of the scattering profiles using a Lorentzian line shape has allowed us to extract structural information on the reconstructed surface. In Sec. III B we shall present the results obtained in different electrolyte solutions in order to understand the effect of the solution species on the electrode structure. The anion species has a marked effect on the phase behavior of the Au(111) surface as a function of potential.

B. The effect of surface charge on Au(111) structure

Previous studies of the Au(111) surface under electrochemical conditions have postulated that the adsorption of anions lifts the $(23\times\sqrt{3})$ reconstruction,[46] but these studies have not been able to demonstrate conclusively the role of anions in this process. In order to separate the role of surface charge density from adsorbate-substrate chemical interactions, we have carried out x-ray-scattering measurements in NaF, NaCl, and NaBr solutions.

Figure 9 shows the potential dependence at $(0.038/\sqrt{3},1+0.038/\sqrt{3},0.2)$ in NaF, NaCl, and NaBr relative to the groomed intensity at a scan rate of 1 mV/sec in both scan directions. The transition potential is in the order $Br^- < Cl^- < F^-$. Furthermore, the hysteresis between the negative and positive sweep directions increases in the same order. For the NaF solutions, there is very little difference between the 0.01- and 0.1-M concentrations. This implies that the double-layer thickness, which varies inversely as the square root of the concentration in the Gouy-Stern-Chapman model,[47] does not affect the potential dependence of the surface structure. The corresponding surface electric field changes by a factor of $\sqrt{10}$ between these two concentrations. In NaCl and NaBr solutions, the phase-transition potential shifts negative and the hysteresis becomes smaller with increasing concentration. These potential shifts are similar to the change in double-layer capacitance observed with different concentrations.[48]

In all three electrolytes, at a sweep rate of 1.0 mV/sec, the reconstruction starts to appear (negative ramp) within

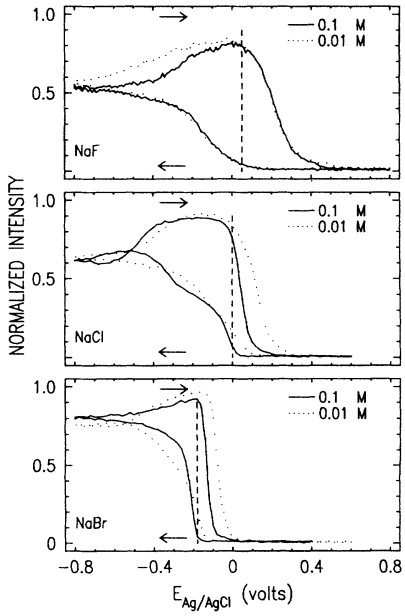

FIG. 9. Potential dependence of the scattering intensity at $(0.038/\sqrt{3},1+0.038/\sqrt{3},0.2)$ in 0.01- and 0.1-M NaF, NaCl, and NaBr solutions at a scan rate of 1 mV/sec in both sweep directions. The potential cycles all originate at a positive potential.

0.1 V of the potential at which the reconstruction starts to lift (positive ramp), as shown in Fig. 9. This critical potential [0.05 V (NaF), 0.0 V (NaCl), and −0.17 V (NaBr)] is indicated by the dashed vertical lines in Fig. 9 for the 0.1-M solutions. Below this potential, the intensity variation with potential depends on kinetic effects (Sec. III C) and grooming. A stable $(23\times\sqrt{3})$ surface reconstruction forms below this critical potential after grooming. Above this critical potential the reconstruction starts to lift and the intensity at $(0.038/\sqrt{3},1+0.038/\sqrt{3},0.2)$ starts to decrease.

In order to demonstrate the relationship between the phase-transition potential with anion adsorption and surface charge, previous interfacial capacitance studies at an Au(111) surface[49,50] are reproduced in Fig. 10(a) on a common potential scale with the x-ray-scattering data in 0.1-M solutions [Fig. 10(b)]. The capacitance-potential curve in dilute nonadsorbing or weakly adsorbing electrolytes exhibits two peaks and the minimum between these peaks is generally accepted as the potential of zero charge (PZC), where there is no excess charge at the metal surface. In NaF solutions, the PZC, 0.37 V (vs Ag/AgCl), has been determined from capacitance measurements.[50] The very slight negative shift in the potential minimum with increasing concentration indicates that the fluoride ions do not significantly adsorb at a gold electrode. On the other hand, there is a marked change in the capacitance with concentration in the NaCl and NaBr solutions. For 0.1-M solutions, the adsorption starts to occur at about −0.10 V for chloride and −0.25 V for bromide, as indicated by the large changes in slope of the capacitance curves as shown in Fig. 10(a).

From the correspondence of the transition potential [Fig. 10(b)] and the peaks in the capacitance data [Fig. 10(a)], the shifts of phase-transition potentials with electrolyte appear to be related to the adsorption of anions [compare Fig. 10(b) with Fig. 10(a)]. However, our data cannot be explained strictly in terms of anion adsorption. For instance, in 0.1-M NaBr, the reconstructed phase is completely stable up to −0.17 V, where the capacitance measurement indicates that a significant amount of Br^- ions have already been adsorbed. In NaF solutions, the lifting of the reconstruction starts at 0.1 V, which is at a featureless region of the capacitance curve and very negative of the PZC (0.37 V), where no F^- ions are adsorbed. In summary, for NaBr the reconstruction is stable with a low Br coverage, whereas in NaF the reconstruction lifts with no F adsorption. This demonstrates that the lifting is indirectly related to anion adsorption.

Second-harmonic-generation measurements at the Au(111) surface[27] in 0.01-M $HClO_4$ have shown that the signal from a reconstructed phase starts to decrease at around 0 V (in the positive-sweep direction). This potential is about 0.35-V negative of the PZC in $HClO_4$. In nonadsorbing KPF_6 solutions, the phase transition also exists in the double-layer potential region as implied by the observed hysteresis in capacitance measurements.[51] These studies support our observations that the phase behavior of the Au(111) surface cannot be explained in terms of anion adsorption alone. We propose instead that the surface structure might be determined by the

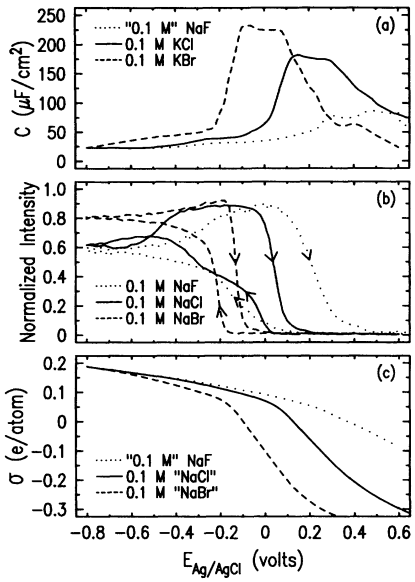

FIG. 10. (a) Capacitance of the Au(111) electrode vs the applied potential. The "0.1-M" NaF curve is derived by averaging capacitance measurements obtained in 0.05- and 0.5-M solutions, because the 0.1-M data are not available in the literature. The 0.05-M NaF data are from Fig. 2 of Ref. 50 and the remaining data are from Fig. 1 of Ref. 49. The potential has been converted from E_{SCE} to $E_{Ag/AgCl}$ by adding 40 mV. (b) Reconstructed scattering density at $(23\times\sqrt{3})$, normalized to the groomed state, vs the applied potential in three 0.1-M solutions. The potential was swept at 1 mV/sec from 0.6 V and switched the direction at −0.8 V. (c) Surface charge density $\sigma(E)$ of the Au(111) electrode in 0.1-M solutions calculated from the capacitance data in (a). It is valid to use the capacitance data obtained in potassium salts for NaCl and NaBr surface-charge curves because both cations are fully hydrated at the interface and do not significantly affect the capacitance curve.

surface charge density, which is a function of both the applied potential and the anion adsorption.

The induced surface charge density versus the applied potential $\sigma(E)$ in NaF solutions has been obtained by integrating the capacitance curve from the PZC to E, that is,

$$\sigma(E)=\int_{\mathrm{PZC}}^{E} C(E')dE' \ .$$

For chloride and bromide solutions, we assume that the surface charge at −0.8 V (where both anions are not adsorbed) is the same as in the NaF solution because the PZC cannot be directly obtained from the capacitance measurements in these two solutions. The results are shown in Fig. 10(c).

The relationship between surface charge and surface reconstruction is displayed in Fig. 11, where the intensity at $(0.038/\sqrt{3},1+0.038/\sqrt{3},0.2)$, acquired as a function of potential, is displayed versus the integrated surface charge for the three 0.1 M solutions in both sweep directions. In all three electrolytes, the transition from the ideally terminated surface to the $(23\times\sqrt{3})$ surface phase occurs at about 0.07 e/atom. A positive electron density (e/atom) corresponds to a net negative charge on the

electrode surface. The discrepancy between the curves above $0.07e$/atom is in part due to kinetic effects which will be discussed further in Sec. III C. In 0.1-M NaF and NaCl electrolytes the reconstruction starts to lift at $\sigma = 0.07e$/atom. This is the same charge density where the reconstruction starts to form. For 0.1-M NaBr the transition is shifted by about 0.02 e/atom, which corresponds to only a 20-mV shift in the applied potential. Within this potential region strong adsorption induces a rapid change in the surface charge density (0.1 e/atom per 0.1 V). In all electrolytes, the reconstruction is nearly completely lifted at zero charge density. Although the three curves in Fig. 11 are not identical, the common features suggests a simple phase-transition mechanism based on the excess surface charge.

In vacuum, a similar surface charge mechanism has been proposed for Ag(110) that reconstructs when a submonolayer of alkali metal is adsorbed.[52] The relative surface energies of the (1×1) and the (1×2) structures as a function of induced charge on the surface have been calculated using local-density-functional theory. The adsorbed alkali-metal ions were modeled by an effective external charge having a negligible overlap with the surface electronic density. Within the context of this model, adsorbates mimic an applied electric field. These theoretical results at the Ag(110) surface[52] suggest that increasing the electron density at the surface favors a more densely packed (reconstructed) surface. Conversely, decreasing the electron density stabilizes the (1×1) structure. Experiments in vacuum have confirmed that surface reconstructions can be lifted by adsorbates that positively charge the surface[53] and, in some cases, reconstructions can be induced by alkali-metal adsorption that negatively charges the surface.[54]

The effect of changes in the surface charge density on the stability of reconstructed surfaces can be related to the electronic origin of spontaneous reconstructions at noble-metal surfaces. Theoretically, it has been suggested that the mobile, delocalized sp electrons in noble metals can assumulate into regions between the surface atoms.[55] This increases the in-plane sp bonding and gives a tangential compressive stress. As pointed out by Smoluchowski,[56] the excess electron density of a negatively charged electrode is accumulated in the valleys between the surface atoms in order to obtain a flat termination of the electronic charge. This smoothing effect leads to an increased sp-electron density between the surface atoms and, hence, to an increased attraction between these atoms which, therefore, show a tendency to form a densely packed reconstruction.[57] Our results at the Au(111) surface are consistent with this mechanism for the electrochemically induced lifting of the surface reconstruction. When the electrode is positively charged, the loss of mobile sp-electron density leads to a weakened attraction between the surface atoms, which makes the reconstruction unstable in comparison to the (1×1) phase. Similar cases have been found in vacuum. For instance, the chemisorption of S and Cl on Ni(001) surfaces[58] shows that the magnitude of the surface Ni-Ni bond strength is insensitive to the strength of the adsorbate-Ni bond. Rather, the Ni-Ni bond strength depends almost exclusively on the adsorbate coverage, which has been related to the total amount of charge removed from the metal surface.

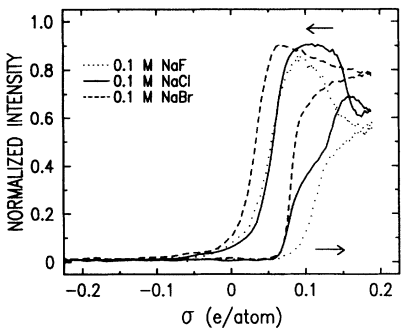

FIG. 11. Scattering intensity of the Au(111) $(23\times\sqrt{3})$ reconstruction vs the induced surface charge derived from the data presented in Fig. 10.

Important features of the Au(111) surface reconstruction phase transition in different electrolytes have emerged when the scattering intensities are plotted versus the surface charge. Our data strongly suggest that the potential-induced reconstruction of the Au(111) surface can be explained in terms of a simple model based on the surface charge. This model explains many of the observed features of the potential dependence of the Au(111) surface in different electrolytes. Additional features of the potential-induced reconstruction are resolved in Sec. III C by considering kinetic effects.

C. Kinetics of the $(1\times1)\leftrightarrow(23\times\sqrt{3})$ phase transitions

The transition between the (1×1) and reconstructed phase of the Au(111) surface has been explored in terms of the applied potential in Secs. III A and III B. In this section we investigate surface structures, as measured by the scattered x rays, as a function of time after a step change in the applied potential. Measurements have been carried out in several solutions to determine (1) the time required to lift the reconstructed surface when the potential is stepped positively, (2) the time required for the reconstruction to recover when the potential is stepped negatively, and (3) the coarsening of the surface structure with time. Comparisons of the measured kinetics in different electrolytes allows us to develop a better understanding of the phase-transition mechanism.

In the first set of measurements, groomed surfaces were prepared by repeated potential cycling in the reconstructed potential regime. After the intensity at $(0.038/\sqrt{3},1+0.038/\sqrt{3},0.2)$ reached 90% of the groomed intensity, the potential was stepped to a positive value from -0.2 V and the scattered intensity was measured versus time.[59] Typical results obtained in 0.01-M NaBr and 0.1-M NaF solutions are shown in Fig. 12. Because of the thin-layer cell geometry, the electrical response time after a potential step at the center of the crystal surface may be as long as 10 sec in 0.01-M electrolyte solutions. In order to minimize this factor, measurements were carried out in 0.09-M NaF supporting elec-

trolytes with 0.01-M NaCl or NaBr. The same time constants were obtained by moving the sample sideways so that the x-ray beam intercepted the edge of the sample, reducing the voltage transmission time to the illuminated sample region. The measurements in 0.01-M NaF solution were carried out in this manner.

In the lifting process, the scattered intensity at $(0.038/\sqrt{3},1+0.038/\sqrt{3},0.2)$ decays exponentially with time if the potential is stepped sufficiently positive. Exponential time constants τ were always found to be at least 2–3 sec. This minimum time constant is about a factor of 5 faster than results obtained from SHG measurements of the Au(111) surface in $HClO_4$ acid solution.[27] In the present measurements, the 2–3 sec time constant may result from the thin-layer cell geometry or it may represent a true kinetic effect of the Au(111) surface. We define a characteristic potential E_{lift} such that for potentials greater than E_{lift} the time constant is less than 3 sec. The results from 0.01- and 0.1-M solutions of sodium halides are listed in Table I. In 0.1-M solutions, the potential E_{lift} is lower than in 0.01-M solutions. Furthermore, this shift with concentration is smallest in NaF solutions and largest in NaBr solutions. In 0.1-M solutions this critical potential corresponds to a surface charge density of about -0.06 e/atom for all three halides. This implies that the lifting process is related to the surface charge density rather than the specifics of the halide-gold interaction.

In the second set of kinetic measurements, we have investigated the growth of the reconstructed Au(111) surface from the (1×1) surface phase in 0.01-M NaCl. The top panel of Fig. 13 shows the intensity at $(0.038/\sqrt{3},1+0.038/\sqrt{3},0.2)$, normalized to the groomed surface, versus time after the potential is stepped from 0.6 V (1×1) phase at $t=0$ sec to E_r (reconstructed) versus time. For consistency, the potential is maintained at 0.6 V for 30 sec before stepping the potential to E_r. The fastest initial growth of the reconstructed phase occurs when the potential is stepped the most negative (Fig. 13, open circles); however, the intensity at $(0.038/\sqrt{3},1+0.038/\sqrt{3},0.2)$ nearly saturates after about 20 sec and only reaches 27% of the maximum value after 120 sec. If, on the other hand, $E_r=-0.3$ V (Fig. 13, solid line), the initial intensity increase is slower but the intensity continues to increase after 20 sec. For $E_r=-0.3$ V the intensity grows to 60% of the groomed value after 120 sec at this potential. These results show that the initial nucleation is faster for the most negative surface charge, whereas the subsequent growth process is favored by a surface charge that is less negative.

TABLE I. The effect of the electrolyte anion on the phase-transition kinetics. The potential E_{lift} corresponds to the minimum potential in which the reconstruction is lifted within 2–3 sec. The potential E_{opt} corresponds to the potential where the reconstruction intensity at $(0.038/\sqrt{3},1+0.038/\sqrt{3},0.2)$ achieves the maximum intensity without surface grooming. The potentials are referred to a Ag/AgCl electrode. The molarity refers to the total halide anion concentration as discussed in the text.

	Molarity	NaF	NaCl	NaBr
E_{lift} (V)	0.01	0.60	0.30	0.20
	0.1	0.55	0.20	−0.05
E_{opt} (V)	0.01	−0.25	−0.30	−0.30
	0.1	−0.15	−0.25	−0.35

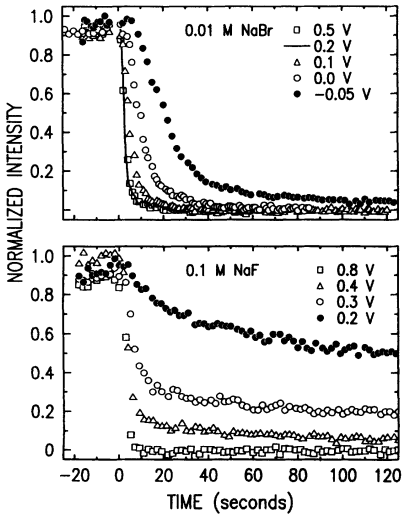

FIG. 12. Time dependence of the reconstruction lifting at several potentials in NaBr (top) and NaF (bottom) solutions. The potential is stepped from −0.2 V to the value indicated for each line at $t=0$ sec.

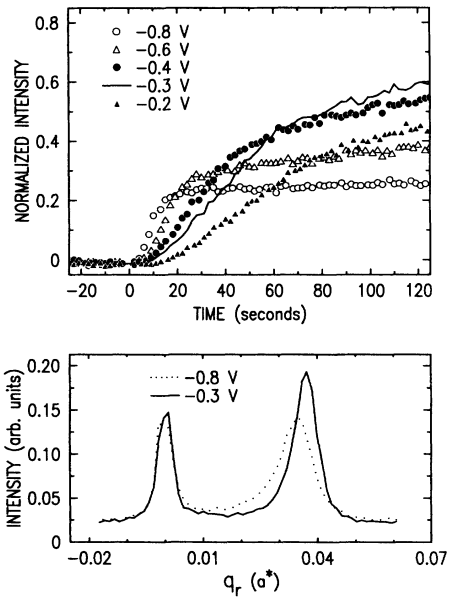

FIG. 13. Top: Time dependence of the reconstruction into $(23\times\sqrt{3})$ for several potentials in 0.01-M NaCl solution after a step change in potential. Bottom: Scattering intensity along the q_r direction measured at 120 sec after a step change in the potential. Note that the reconstruction is better formed at −0.3 V than at −0.8 V.

In order to ascertain how different potential conditions affect the structure of the (1×1) to $(23\times\sqrt{3})$ phase transition, scans were performed along q_r at 200 sec after stepping the potential to E_r. Fits of the scattering profiles to Eq. (4) show that the surface is most compressed at $E_r=-0.3$ where the fit yields $p=24.0$ and $\zeta_\delta=41.4a$. At $E_r=-0.8$ the surface is less compressed and the fit yields $p=26.2$ and $\zeta_\delta=25.7a$. The factor of 2 difference in the intensity between these two voltages (see Fig. 13) at $t=120$ sec is accounted for by an increase in ζ_δ and a shift in p.

The formation of the reconstructed phase, after a step change in potential, can be described by a spontaneous nucleation process followed by a much slower process that involves the cooperative behavior of many surface atoms in order to form large domains with the optimal packing density (i.e., $p=23$). The latter process is controlled by the mobility of surface gold atoms, which is the slowest at the most negative potentials. The kinetic behavior (discussed above) and the improved surface order with potential cycling suggests that the fastest approach to a well-ordered reconstructed phase cannot be obtained at a fixed surface charge (potential). Whereas the driving force for reconstruction [the decrease of free energy of the reconstructed phase relative to the (1×1) phase] increases with decreasing potential, the mobility of gold atoms increases with increasing potential.[60,61] From these two considerations, there is an optimal potential $E_{\rm opt}$, where the reconstructed domains reach a most ordered state as determined by the x-ray intensity (Fig. 13). In all cases, the intensity is smaller than the groomed intensity.

The measured values of $E_{\rm opt}$ are summarized in Table I for the three electrolytes with 0.01- and 0.1-M concentrations. In 0.1-M solution the optimal potentials are -0.15 V (NaF), -0.25 V (NaCl), and -0.35 V (NaBr). In these three electrolytes, the potential $E_{\rm opt}$ corresponds to about the same value of the surface charge density (0.12 e/atom). However, at 120 sec after stepping the potential to $E_{\rm opt}$ in 0.1-M solutions, the intensity at $(0.038/\sqrt{3},1+0.038/\sqrt{3},0.2)$, relative to the groomed intensity, is 80% for NaBr, 65% for NaCl, and 60% for NaF. At $E_{\rm opt}$, the capacitance curves indicate that a small amount of chloride and bromide are adsorbed on the surface as shown in Fig. 10(a). The adsorption of trace amounts of chloride and bromide anions improves the surface mobility,[60,61] which significantly decreases the formation time to the reconstructed surface state.

In the third set of kinetic measurements we have investigated the temporal evolution of the scattering line shape on the second time scale after a step change in potential. These measurements were carried out at X25 at $\lambda=1.18$ Å. The scans along q_r, reported in Fig. 5, required several minutes and were too slow to measure the early stages of the nucleation and growth phenomena. To obtain the scattering profiles versus time we take advantage of the fact that the surface can be repetitively cycled between the reconstructed and the (1×1) state and that the average surface structure undergoes the same evolution for all cycles. In Fig. 14(a) we show a repetitive cycle where the potential is stepped to 0.5 V (1×1) at 0 sec and to -0.3 V (reconstructed) at 20 sec. During each potential cycle, the scattered intensity is acquired versus time at a fixed q_r. After every potential cycle the position along q_r is incremented and the standard potential cycle is resumed by stepping the potential to 0.5 V. In this manner, we are able to acquire a reciprocal space-time scattering profile. The equal intensity contours are displayed in Fig. 14(b).

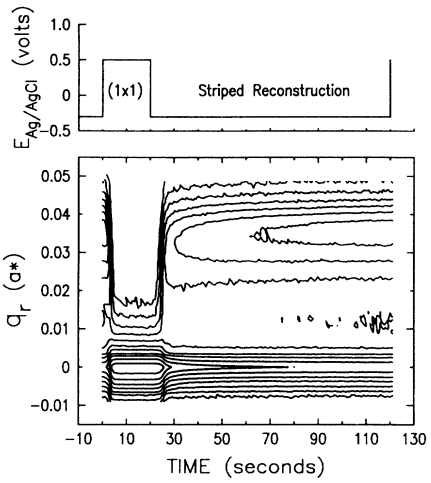

FIG. 14. Top: Repetitive potential cycle where the voltage is stepped to 0.5 V (1×1) at 0 sec and to -0.3 V (reconstructed) at 20 sec and back to 0.5 V after 120 sec. Bottom: Geometric density contours in a q_r and time plane in a mixture of 0.01-M NaCl and 0.49-M NaF electrolytes where the potential dependence is given in (a). Adjacent contour lines differ by a factor of 0.65. Within several seconds after raising the potential to +0.5 V, the intensity contours associated with the reconstructed phase vanish and there is a subsequent increase in the intensity at $q_r=0$. About 5 sec after the potential is lowered to -0.3 V there is a rather uniform increase in the scattered intensity all the way from $q_r=0.01a^*$ until $0.05a^*$ with no apparent peak.

In order to improve the time response in the thin-layer geometry we have carried out the measurements in a mixed solution containing 0.01-M NaCl in a 0.49-M NaF solution. The high NaF concentration reduces the cell resistance (R), and decreases the time constant of the cell. The potential dependence of the scattering from the Au(111) surface, at $q_r=0.038a^*$, in the mixed solution is virtually identical to the result obtained in 0.01-M NaCl at a 1-mV/sec scan rate.

Within several seconds after raising the potential to +0.5 V, the intensity contours associated with the reconstructed phase vanish and there is a subsequent increase in the intensity at $q_r=0$. About 5 sec after the potential is lowered to -0.3 V there is a uniform increase in the scattered intensity all the way from $q_r=0.01a^*$ until $0.05a^*$ with no apparent peak. We associate this behavior with a disordered phase in which an ordered stripe separation has not been established. At about 10 sec after lowering the potential to -0.3 V, an ordered striped phase starts to establish, yet the measured line shape is broad. As the reconstruction develops the intensity in the wings of the scattering profiles remain fixed,

whereas the peak intensity continues to increase. Analysis of the scattering profiles in Fig. 14 at fixed time indicates that there is a factor of 3 increase in the fitted correlation length in going from $t=30$ to 120 sec.

In the nucleation and growth process of the $(23\times\sqrt{3})$ reconstruction, it is important to consider the effects of the three symmetry-equivalent directions for the uniaxial compression that are rotated from each other by $\pm 120°$. Spontaneous nucleation and growth conditions should populate the surface with random domains of these three orientations. The collision between growing domains with different orientations develops a random array of kink dislocations at the electrode surface. This is in contrast to the Au(111) surface in vacuum, after cycling to high temperatures, where the surface exhibits a regular array of kink dislocations in a zig-zag pattern.[8,31,32] Under these conditions, the kink density is related to the inverse domain size. Whereas kinks in the discommensuration direction reduce the substrate strain energy, an overabundance of kinks increases the high-energy domain-wall boundary regions. This argument suggests that there is an optimal density of kinks. If the density of nucleating sites is larger than the optimal kink density, and if these kinks are not mobile, then the electrode surface cannot reach the most ordered state. The grooming process may facilitate a rearrangement of the kinks to form a structure with the optimal kink density.

These measurements of the time evolution of the scattering provide complementary information on the transition between the ideally terminated (1×1) surface and the $(23\times\sqrt{3})$ reconstructed surface. Analysis of the temporal data suggests that the effects of surface mobility and the energy difference between the two phases (driving force) play an important role in the phase transition.

D. Surface-normal structure — reconstructions, anion adsorption, and surface water

In this section, we demonstrate that the surface-normal structure at the electrode/electrolyte interface can be determined from the scattering profiles along the surface-normal direction. Reflectivity refers to the absolute scattered intensity, normalized to the incident flux,[62] along the surface-normal direction at fixed in-plane wave vectors. The experimental configuration for the reflectivity measurements is identical to previous studies at the vacuum interface that have been reported elsewhere.[13] Briefly, the reflectivity measurements were obtained by setting the spectrometer to L and integrating the reflected signal in a θ scan. In this procedure, the data were corrected for background contributions and the incident x-ray polarization.[13]

In Fig. 15, the specular x-ray reflectivities are shown in KBr (top, $\times 10000$), NaCl (middle, $\times 100$), and NaF electrolytes along with several model curves between $L=0.2$ and 6.5. The latter two measurements were carried out at $\lambda=1.24$ Å and the KBr measurement was carried out at $\lambda=1.54$ Å. Near $L=0$, 3, and 6 ($H=K=0$) there is a rapid increase in the scattered intensity and the latter two peaks correspond to the cubic (1,1,1) and (2,2,2) Bragg reflections. Between these peaks the observed reflectivity is weak and depends on the detailed structure of the interface. The specular reflectivity from the reconstructed surface (open symbols) exhibits an overall asymmetry in the wings of the (0,0,3) and (0,0,6) Bragg peaks, being larger at smaller wave vectors. To within our statistics, the specular reflectivities for the reconstructed surfaces in all three solutions and in $HClO_4$ have similar line shapes, independent of potential. This is because the cations are not directly bound to the surface. On the other hand, the reflectivity profile obtained in the (1×1) potential region (filled symbols) varies with the anion species as shown in Fig. 15. We note that the calculated specular profile for an ideally terminated Au(111) surface [Eq. (3)], shown as dotted lines in Fig. 15, does not adequately describe the reflectivity over the entire range of L for any of the solutions.

Further evidence of anion adsorption effects on the specular reflectivity is presented in Fig. 16, where the potential dependence of the effective specular reflection[63] at a fixed position, (0,0,2.2), is shown. These curves were obtained in 0.01-M solution of KBr, NaCl, and NaF at a

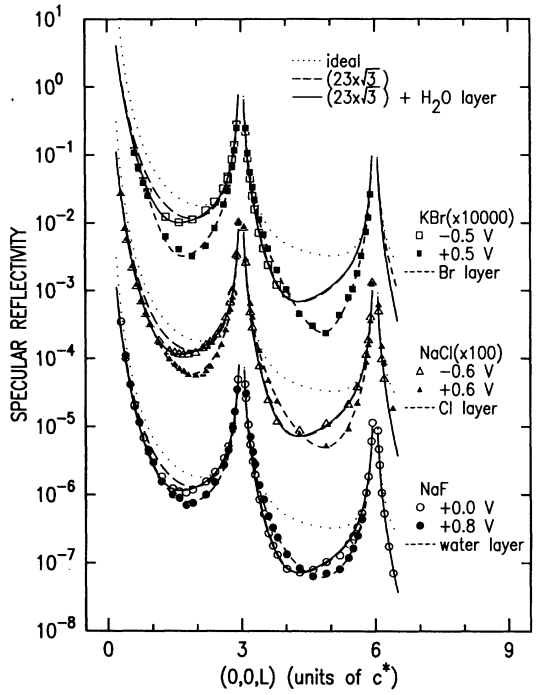

FIG. 15. Absolute specular x-ray reflectivity from the Au(111) surface in 0.01-M solutions of KBr (top, $\times 10000$), NaCl (middle, $\times 100$), and NaF(bottom). The open symbols correspond to the $(23\times\sqrt{3})$ reconstructed phase and the filled symbols correspond to the (1×1), surface phase. The reflectivity profile for a reconstructed phase in vacuum is shown as the long-dashed line. The reconstructed reflectivity profile under electrochemical conditions with an adsorbed water layer is shown as the solid line and deviates from the vacuum model around $L=1$. Above $L\approx3$ the long-dashed and solid lines merge. The ideally terminated (1×1) surface reflectivity is shown as the dotted line. Fits to the KBr, NaCl, and NaF reflectivities at 0.5, 0.6, and 0.8 V, respectively (solid symbols) are shown as the short-dashed lines.

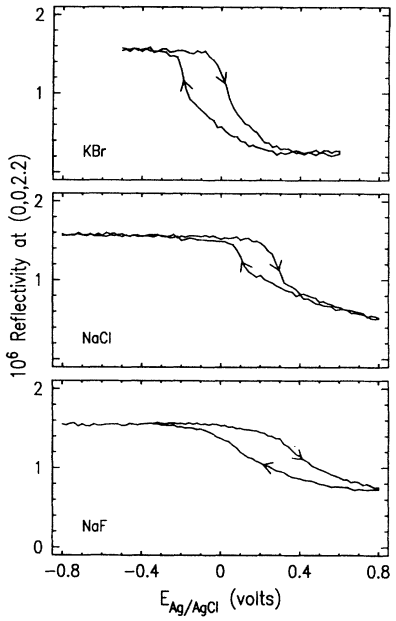

FIG. 16. Potential dependence of the reflectivity at (0,0,2.2) on an absolute scale in 0.01-M solutions of KBr, NaCl, and NaF in the positive and negative sweep directions. The potential independent reflectivity at low potentials corresponds to the reconstructed phase. The decrease in intensity at high potentials corresponds to the transition to the (1×1) state and anion adsorption.

slew rate of 1 mV/sec in both sweep directions. Scans at $(0,0,\frac{3}{2})$, exactly halfway between the (0,0,0) and (0,0,3) Bragg peaks, exhibit very similar potential dependence to those at (0,0,2.2). At the most negative potentials the surface is reconstructed (as discussed in Sec. III B) and the absolute reflectivity equals $1.56\pm0.05\times10^{-6}$ in all three solutions. The decrease in the reflectivity at (0,0,2.2) results from the transition from the reconstructed phase to the (1×1) phase and from the adsorption of anions at the gold interface. This intensity decrease is the greatest in the KBr electrolyte, since the adsorbed bromide ions have the largest number of electrons, i.e., the largest scattering amplitude, compared with chloride and fluoride. Above 0.3 V the intensity decrease levels off where the adsorbed bromide layer saturates (a decrease in the capacitance), as shown in Fig. 10(a). In NaCl solution, the capacitance peak extends beyond 0.3 V, which implies that the adsorbed chloride layer is not saturated up to 0.3 V. Correspondingly, the reflectivity at (0,0,2.2) continues to decrease as the potential is extended beyond 0.3 V as more chloride is adsorbed. Because the adsorption-desorption of anions at the gold surface is reversible and occurs rapidly upon changing the potential, the reflectivity versus potential curves obtained from both sweep directions overlap at the potentials above 0.3 V. In order to account for the effects of solution species at the gold interface and potential-induced changes in the structure of the gold layers, the reflectivity model given by Eq. (3) must be extended.

A realistic description of reconstructed gold surfaces in vacuum requires a modification of the sum over atomic layers to allow for variations in the layer spacing, layer densities, and enhancements of the root-mean-square displacement amplitudes.[8,13,42] In addition, the effects of the solution species at the interface must be included. To accommodate these effects, we express the specular reflectivity as

$$R(0,0,L)=|T(Q_z)|^4\left[\frac{256\pi^2r_0^2}{3a^2Q_z^2}\right]|s(0,0,L)|^2e^{-Q_{\rm abs}/Q_z}\ , \tag{5a}$$

where the sum over atomic layers is

$$s(0,0,L)=Z_0\langle\rho_0e^{-Q_z^2\sigma_0^2/2}e^{iQ_zd_0}\rangle + F_{\rm Au}(Q_z)\sum_{n=1}^{\infty}\langle\rho_ne^{-Q_z^2\sigma_n^2/2}e^{iQ_zd_n}\rangle\ . \tag{5b}$$

The first term in Eq. (5b) corresponds to the scattering amplitude from a surface ion-water monolayer with a molecular charge Z_0 (fixed in the analysis), an atomic layer density ρ_0 relative to a Au(111) atomic layer, and a root-mean-square (rms) atomic displacement σ_0 along $\hat{n}$. The second term corresponds to the sum over gold layers. The gold atomic surface-normal displacement amplitude σ_n is enhanced at the surface over the bulk thermal Debye-Waller value of 0.085 Å.[65] Surface enhancements in σ_n, relative to the bulk value, have a pronounced effect on the specular and nonspecular reflectivities when the surface-normal wave vector, i.e., L, is far from a Bragg peak, but a minimal effect near Bragg peaks. In the bulk, the atomic layers are positioned at nd, whereas, at or near a surface the interlayer atomic spacing may either expand or contract. This relaxation produces an asymmetric reflectivity—along L—in the wings of the Bragg peaks. For an interlayer expansion of the topmost gold layer, the reflectivity is increased at wave vectors just below the peak and the reflectivity decreases at wave vectors just above the peak.[42] In order to account for the absorption losses from the polypropylene window and the capillary electrolyte layer we have assumed a slab of adsorbing material of constant thickness. This produces the factor $e^{-Q_{\rm abs}/Q_z}$, where $Q_{\rm abs}$ is related to the thickness, density and mass absorption cross sections of these layers.[20]

In the subsequent analysis, the absorption correction given in Eq. (5a), $Q_{\rm abs}$, is fixed at a value of $0.2c^*$ for the NaF and NaCl data and at a value of $0.4c^*$ for the KBr data, because a lower-energy x-ray beam was used in the KBr measurements. This provides a reasonable description of the small-wave-vector reflectivity where absorption effects dominate. Reflectivity within $0.05c^*$ of the Bragg peaks and below $0.4c^*$ has been excluded from the fitting procedure. In the first case, the kinematic approximation does not apply near Bragg peaks and in the latter case it is difficult to control the footprint of the incident beam on the sample at small angles.

In order to understand the effects of adsorbed species at the Au(111) surface, it is useful to compare directly the electrochemical results with results from clean vacuum

surfaces. Since both the vacuum and electrochemical data support the same $(23\times\sqrt{3})$ motif we believe that the scattering from the gold layers should be the same for both interfaces. Differences in these specular reflectivities can be accounted for by adsorbed species at the interface. In vacuum at $T=300$ K, the specular reflectivity is well described by a real-space atomic model[8] with $\sigma_1=0.13$ Å, $\rho_1=1.045$, and a relative interlayer expansion of the top gold layer, $\varepsilon_1=(d_1-d_2)/d_{\text{bulk}}-1=3.3\%$. The remaining parameters are fixed at their "bulk ideal values." This model, shown as a dashed line in Fig. 15, provides a reasonable description of the reconstructed reflectivity in all three electrolytes (open symbols) above $L=3$ but fails to describe the data between $L=0.5$ and 2.5.

An improved description of the specular reflectivity, in the reconstructed potential range for all three electrolytes is obtained if we incorporate an ordered water layer. In the analysis, we have fixed the molecular charge $Z_0=10$ (water). The parameters for the top gold layer were set to values obtained in vacuum ($\rho_1=1.045$ and $\varepsilon_1=3.3\%$),[8] and we have allowed ρ_0, d_0, and σ_0 to vary. All three data sets are very well described by a model with $\rho_0=1.0\pm2$, $\sigma_0=0.35\pm0.1$ Å, and a gold-water distance of 2.9 ± 0.3 Å given by the solid lines in Fig. 15. A density of $\rho_0=1.0$ for water only represents 13% of the electron density for the underlying gold layers. This water density is larger than the expected layer density (0.75) calculated from the water volume (30 Å^3 per water molecule) raised to the $\frac{2}{3}$ power. One possibility is that small monolayer-height gold clusters, which occupy a small fraction of the surface area, could also lead to a diminished reflectivity between the Bragg peaks. By incorporating gold clusters covering 3–4 % of the gold surface, it is possible to use a water layer with a coverage of 0.75. Alternatively, incorporating both a first and second water layer improves the description of the data. The best fit is obtained with first and second water-layer densities of 0.7 and 0.3, respectively, relative to the gold-layer densities. From the reflectivity profiles at fixed potentials it is difficult to distinguish between water and solution species, since both contribute to the electron densities of the solution layers.

The present analysis of the reflectivity profiles supports the standard model of the electrochemical double layer. Within the context of this model, cation ions are attracted to the negatively charged metal surface but remain hydrated. This implies that the metal surface is only in direct contact with water molecules (no specific adsorption) and that the second solution layer is composed of both cation species and water molecules. Within the context of our two-layer fit, the second-layer density (0.3) may in part result from solvated sodium ions which are at a well-defined distance from the charged electrode surface. This model suggests that the water in the second layer and beyond are more disordered in the surface-normal direction than either the first water layer or the cations in the second layer. The adsorption of a hydrated cesium ion has a significant impact on the reflectivity profiles, since the charge of a cesium cation (54 electrons) is much greater than for a sodium cation. For instance, in 0.01-M CsCl at (0,0,2.2) the reflectivity reversibly increases within the reconstructed potential regime, when the potential is lowered (increased coverage). In contrast, an increase in the coverage of chloride ions that are directly adsorbed to the gold surface leads to a decrease in the reflectivity at (0,0,2.2). Detailed modeling suggest that the Cs^+ ions are present in the second layer rather than in the first layer. Measurements of the potential dependence of the reflected intensity at wave vectors smaller than that at (0,0,2.2) should be more sensitive to the cation coverage in the second layer, according to Eq. (5).

The present model of the specular reflectivity [Eq. (5)], including the effects of a water monolayer, also describes the reflectivity from the Au(111) surface in the (1×1) phase at positive potentials in NaF. Within the context of this model, the best fit is represented by a gold-water layer spacing of 2.9 Å, an rms displacement amplitude of the water layer, $\sigma_0=0.37$ Å, and a water layer density of 1.0 ± 0.2. There is no apparent relaxation of the top gold-gold interlayer spacing and the rms displacement amplitude of the top gold layer σ_1 is 0.10 Å in the (1×1) potential regime. Extending the model to include a second water layer does not improve the quality of the fit and suggests that the first-layer density is close to unity. This density is higher than the expected density of 0.75 (see above) and this discrepancy may result from gold clusters or from directly adsorbed fluoride ions.

The specular reflectivity profiles for the Au(111) electrode in the (1×1) potential region in KBr (0.5 V) and NaCl (0.6 V) have been fitted with the same single-layer model with Z_0 fixed at 36 and 18 for the bromide and chloride anions, respectively. In the analysis, we allowed the three additional parameters describing the adsorbed anion layer (ρ_0, d_0, and σ_0) and the parameters describing the top gold layer (σ_1 and d_1) to vary in the least-squares-fitting procedure. All of the remaining parameters have been constrained at their bulk values. The best fits for the NaCl and KBr specular reflectivities (short dashed line in Fig. 15) provide an excellent description of the reflectivity profiles. The fitted model is described by an anion layer with rms displacement amplitudes (σ_0) of 0.27 Å (bromide) and 0.28 Å (chloride). The fitted atomic-layer densities (ρ_0) are 0.49 (bromide) and 0.64 (chloride). These densities are calculated relative to the atomic density of a Au(111) layer which is 1.39×10^{15} *atoms/cm*^{2}. These values imply densities of 6.8×10^{14} *bromide atoms/cm*^{2} (0.01*M* KBr at 0.5 V), and 8.9×10^{14} *chloride atoms/cm*^{2} (0.01*M* NaCl at 0.6 V). These numbers are in close agreement with the ESCA studies on emersed polycrystalline gold electrode from bromide and chloride solutions.[65] In both electrolytes the rms displacement amplitudes of the top gold layer, $\sigma_1=0.12$ Å, is slightly smaller than the reconstructed value. The gold-bromide and gold-chloride layer spacings are 2.4 ± 0.3 Å and are larger than the gold-gold layer spacing. Finally, we note that there is no apparent relaxation of the gold-gold layer spacing for the top gold layer (within 0.5%).

We now turn our attention to the nonspecular reflectivity profiles. In Fig. 17 nonspecular reflectivity

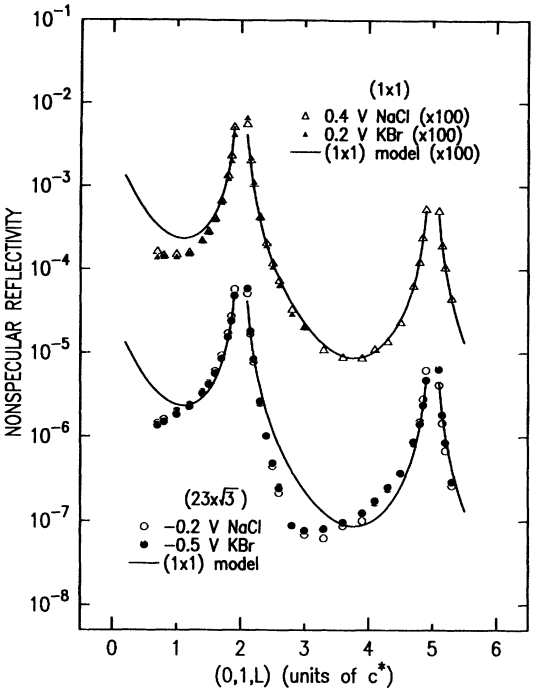

FIG. 17. Nonspecular x-ray reflectivity $(0,1,L)$ from the Au(111) surface in 0.01-M solutions of KBr and NaCl obtained using a symmetric mode ($\alpha=\beta$) at 1.54 Å. The solid line corresponds to an ideally terminated (1×1) model and agrees with the high potential data ($\times100$) in both solutions shown as the triangles.

profiles $(0,1,L)$ are shown for 0.01-M solutions of KBr (filled symbols) and NaCl (open symbols). Peaks in the reflectivity are observed at (0,1,2) and (0,1,5) corresponding to the cubic reflection (0,0,2) and (1,1,3), respectively. Whereas the reflectivity profiles within the (1×1) potential region differ from the NaCl and KBr electrolytes, the nonspecular reflectivities are the same in both solutions, independent of potential, within the same potential range. The latter motion is supported by the potential scan at the (0,1,0.5) position shown in Fig. 7(b). The flat feature at positive potentials before and after the sharp changes due to the phase transitions suggests that adsorbed chloride ions do not affect the nonspecular reflectivity.

Theoretically, the nonspecular reflectivity, along L at (H,K), can be expressed as[13]

$$R(H,K,L)=|T(Q_z)|^4\left[\frac{256\pi^2r_0^2}{3a^2Q_z^2}\right]\times|s(H,K,L)|^2e^{-Q_{\rm abs}/Q_z}\,, \tag{6a}$$

where the sum over atomic layers is

$$s(H,K,L)=F_{\rm Au}(Q_z)\sum_{n=1}^{\infty}\langle\rho_n^{(H,K)}e^{-Q_z^2\sigma_n^2/2}e^{iQ_zd_n}\rangle\,, \tag{6b}$$

where we have ignored the effects of solution species at the interface ($n=0$). In this expression, relative to Eq. (5), the layer density ρ_n has been replaced by the layer-dependent crystalline order parameter $\rho_n^{(H,K)}$, which corresponds to the amplitude of the electron density wave for the nth layer at an in-plane position (H,K). The crystalline order parameter for integers H and K—except for (0,0)—measures the extent to which the gold layers are in registry with the underlying bulk layers at (H,K). For reconstructed surfaces, not all of the gold surface atoms ($n=1$) are in registry with the Au(111) lattice positions and $\rho_1^{(H,K)}$ is less than unity. This effect reduces the reflectivity between adjacent nonspecular Bragg peaks relative to an ideally terminated surface.[8,13]

The solid line corresponds to the calculated reflectivity for a perfectly terminated lattice calculated from Eq. (6) with no interlayer expansion for the top gold layer and no adsorbed electrolyte layer. This provides an excellent description of the nonspecular reflectivity above $L=2$ in both the NaCl and KBr electrolytes at 0.4 and 0.2 V, respectively, and supports our contention that above the phase-transition potential, the surface indeed exhibits a (1×1) phase. Deviations at small L may result from absorption effects and limitations in the present integration procedure. Similar deviations are exhibited in the reconstructed phase under vacuum conditions.[8]

At negative potentials, where the Au(111) surface exhibits a $(23\times\sqrt{3})$ reconstruction, the reflectivity profiles cannot be described by the ideally terminated Au(111) crystal. Rather, the profiles exhibit asymmetric wings around the (0,1,2) and (0,1,5) Bragg peaks. The asymmetry is similar to the asymmetry in the specular reflectivity in the $(23\times\sqrt{3})$ potential regime (open symbols in Fig. 15). Our nonspecular reflectivity data are virtually identical to the nonspecular reflectivity obtained under vacuum conditions[8] at $T=300$ K and requires a model with $\rho_1^{(0,1)}\sim0.7$. This value is consistent with a reconstructed phase in which the surface stacking sequence changes from ABC to ABA, as shown in Fig. 1.[8] The agreement between the vacuum and electrochemical nonspecular reflectivity profiles suggests that the gold surface-normal structure is the same for these differing environments.

Specular reflectivity in the reconstructed phase suggests that there is a well-defined monolayer of water at the interface. In the (1×1) phase, the adsorption of anions has a drastic effect on the reflectivity and detailed analysis provides information on the coverage and position of this anion layer. Finally, nonspecular reflectivity confirms that the phase transition from the $(23\times\sqrt{3})$ phase at low potential is to an ideally terminated, (1×1) phase at higher potential.

IV. SUMMARY

In this paper we have presented the results of *in situ* structural x-ray-scattering studies of the Au(111) electrode surface in NaF, NaCl, LiCl, CsCl, and NaBr solutions. The top layer of gold atoms undergoes a reversible phase transition between the (1×1) bulk termination and a $(p\times\sqrt{3})$ uniaxial discommensuration (striped) phase on changing the electrode potential. Below a critical potential in all solutions, $p=23$ is identical to results obtained in vacuum. However, an ordered array of discommensuration kinks is not observed. The reconstruction is par-

tially lifted with $23 < p < 30$ above this critical potential. At sufficiently positive potentials the striped phase disappears and the surface exhibits the structure of a (1×1) surface. The reconstruction reforms from the (1×1) phase at potentials below the critical potential. Anion adsorption shifts the critical potential and modifies the reconstruction kinetics.

Comparison of the phase-transition behavior in different halide solutions supports a unifying model based on the surface charge density. The critical potentials in 0.1-M NaF, NaCl, and NaBr solutions correspond to the same surface charge density of 0.07 *e*/atom (negatively charged). The complete lifting of the reconstruction occurs at a potential corresponding to zero surface charge in all electrolytes. Furthermore, both the minimum potential of instant lifting, E_{lift}, and the optimal potential for reforming the reconstruction, E_{opt}, have the same surface charge densities -0.06 and 0.12 *e*/atom, respectively, in all solutions. Therefore, the surface charge density plays an important role in the phase behavior of Au(111) electrode surface.

The kinetics of the phase transitions involves the potential dependence of the driving force [energy difference between the (1×1) and the $(23\times\sqrt{3})$ phases] and surface mobility. The reconstructed phase disappears within several seconds after stepping the potential from the reconstructed potential region to a potential above E_{lift}. Spontaneous nucleation of the reconstructed phase occurs across the entire surface when the potential is stepped from the (1×1) potential regime to a potential in the reconstructed potential region. Since the driving force for the surface reconstruction increases with increasing surface electron density, the fastest initial growth occurs at the most negative potential. The mobility of the surface atoms decreases with increasing negative charge on the surface. This explains why the reconstruction growth process "turns off" at the most negative potentials before a well-ordered, reconstructed surface is formed. Cycling the potential in the reconstructed regime gives the most-ordered reconstructed surface.

Complementary information on the Au(111) surface has been obtained by carrying out x-ray-reflectivity measurements to determine the surface-normal electron density profile at the gold/electrolyte interface. In the $(23\times\sqrt{3})$ phase, the interlayer spacing of the top gold layer is expanded by 3.3% relative to the bulk layer spacing. There is no interlayer relaxation of the top gold layer in the (1×1) phase. At potentials where there is no specific adsorption of ions, our data supports a well-defined monolayer layer of water at the gold interface. Adsorbed chloride and bromide monolayers (Stern layers) have a pronounced effect on the specular reflectivity profiles.

ACKNOWLEDGMENTS

We would like to thank Alan Gibaud for his participation in the early stages of these measurements. We have benefited from discussions with Lonny Berman, Robert Feidenhansl, Doon Gibbs, Joe Gordon, Antionette Hamelin, Jim McBreen, Simon Mochrie, Ian Robinson, Alex Sandy, Bruce Schardt, Michael Toney, Michael Weinert, and Andrzej Wieckowski. This work has been supported by an exploratory research grant at Brookhaven National Laboratory and by the Division of Materials Research, U.S. Department of Energy, under Contract No. DE-AC02-76CH00016.

[1]M. A. Van Hove, R. J. Koestner, P. C. Stair, J. B. Biberian, L. L. Kesmodel, I. Bartos, and G. A. Somarjai, Surf. Sci. **103**, 189 (1981); **103**, 218 (1981).

[2]D. M. Kolb and J. Schneider, Electrochim. Acta **31**, 929 (1986); P. N. Ross and A. T. P'Agostino, *ibid.* **37**, 615 (1992).

[3]J. Perdereau, J. P. Biberian, and G. E. Rhead, J. Phys. F **4**, 1978 (1974).

[4]D. M. Zehner and J. F. Wendelken, *Proceedings of the Seventh International Vacuum Congress and the Third International Conference on Solid Surfaces, Vienna, 1977* (F. Berger and Sohne, Vienna, 1977), p. 517.

[5]K. Yamazaki, K. Takayamagi, Y. Tanishiro, and K. Yagi, Surf. Sci. **199**, 595 (1988).

[6]U. Harten, A. M. Lahee, J. Peter Toennies, and Ch. Woll, Phys. Rev. Lett. **54**, 2619 (1985).

[7]K. G. Huang, D. Gibbs, D. M. Zehner, A. R. Sandy, and S. G. J. Mochrie, Phys. Rev. Lett. **65**, 3317 (1990).

[8]A. R. Sandy, S. G. J. Mochrie, D. M. Zehner, K. G. Huang, and D. Gibbs, Phys. Rev. B **43**, 4667 (1991).

[9]I. K. Robinson, Phys. Rev. Lett. **50**, 1145 (1983).

[10]G. Binning, H. Rohrer, C. Gerber, and E. Weibel, Phys. Rev. Lett. **49**, 57 (1982).

[11]S. G. J. Mochrie, D. M. Zehner, B. M. Ocko, and D. Gibbs, Phys. Rev. Lett. **64**, 2925 (1990).

[12]D. Gibbs, B. M. Ocko, D. M. Zehner, and S. G. J. Mochrie, Phys. Rev. B **42**, 7330 (1990).

[13]B. M. Ocko, D. Gibbs, K. G. Huang, D. M. Zehner, and S. G. J. Mochrie, Phys. Rev. B **44**, 6429 (1991).

[14]R. Sonnenfeld, J. Schneir, and P. K. Hansma, in *Modern Aspects of Electrochemistry,* edited by J. O'M. Bockris (Plenum, New York, 1990), Vol. 21.

[15]H. Siegenthaler and R. Christoph, in *Basic Concepts and Application of Scanning Tunneling Microscopy,* edited by H. Rohrer, R. J. Behn, and N. Garcia (Kluwer, Dordrecht, 1990).

[16]D. J. Trevor, C. E. Chidsey, and D. N. Loiacono, Phys. Rev. Lett. **62**, 929 (1989).

[17]S. Yau, X. Gao, S. C. Chang, B. C. Schardt, and M. Weaver, J. Am. Chem. Soc. **113**, 6049 (1991).

[18]X. Gao, A. Hamelin, and M. J. Weaver, Phys. Rev. Lett. **67**, 618 (1991).

[19]C. Chen and A. A. Gewirth, Phys. Rev. Lett. **68**, 1571 (1992).

[20]B. M. Ocko, J. Wang, A. Davenport, and H. Isaacs, Phys. Rev. Lett. **65**, 1466 (1990).

[21]M. F. Toney *et al.*, Langmuir **7**, 796 (1991), and references therein.

[22]M. G. Samant, M. F. Toney, G. L. Borges, L. Blum, and O. R. Melroy, J. Phys. Chem. **92**, 220 (1988).
[23]J. Wang, A. Davenport, H. Isaacs, and B. M. Ocko, Science **255**, 1416 (1992).
[24]B. M. Ocko, A. Gibaud, and J. Wang, J. Vac. Sci. Technol. A (to be published).
[25]A. Hamelin, J. Electroanal. Chem. **142**, 299 (1982).
[26]J. P. Bellier and A. Hamelin, C. R. Acad. Sci. Ser. C **280**, 1489 (1975).
[27]A. Friedrich, B. Pettinger, D. M. Kolb, G. Lupke, R. Steinhoff, and G. Marowsky, Chem. Phys. Lett. **163**, 123 (1989).
[28]G. Lüpke, G. Marowsky, R. Steinhoff, A. Friedrich, B. Pettinger, and D. M. Kolb, Phys. Rev. B **41**, 6913 (1991).
[29]N. J. Tao and S. M. Lindsay, J. Appl. Phys. **170**, 5143 (1991).
[30]X. Gao, A. Hamelin, and M. J. Weaver, J. Chem. Phys. **95**, 6993 (1991).
[31]J. V. Barth, H. Brune, G. Ertl, and R. J. Behm, Phys. Rev. B **42**, 9307 (1990).
[32]D. D. Chambliss and R. J. Wilson, J. Vac. Sci. Technol. B **9**, 928 (1991).
[33]J. L. Whitton and J. A. Davies, J. Electrochem. Soc. **111**, 1347 (1964).
[34]Microelectrodes, Inc., 302 Rockingham Road, Londonderry, NH 03053.
[35]Millipore Q water system, Millipore Corp., P.O. Box 435, Ridgefield, NJ 07657.
[36]Aldrich Corp., 940 West Saint Paul Avenue, Milwaukee, Wisconsin 53233.
[37]Matheson Corp., P.O. Box 8247, Ward Hill, MA 01835-0747.
[38]W. R. Busing and H. A. Levy, Acta Crystallogr. **22**, 454 (1967).
[39]J. Bohr, R. Feidenhans'l, M. Nielsen, M. Toney, R. L. Johnson, and I. K. Robinson, Phys. Rev. Lett. **54**, 1275 (1985).
[40]B. E. Warren, *X-ray Diffraction* (Addison-Wesley, Reading, MA, 1969).
[41]I. K. Robinson, Phys. Rev. B **33**, 3830 (1986).
[42]D. Gibbs, B. M. Ocko, D. M. Zehner, and S. G. J. Mochrie, Phys. Rev. B **38**, 7303 (1988).
[43]A. Braslau, P. S. Pershan, G. Swislow, B. M. Ocko, and J. Als-Nielsen, Phys. Rev. A **38**, 2457 (1988).
[44]This was carried out by using a Ge(111) analyzer rather than Soller slits.
[45]O. L. Alerhand, D. Vanderbilt, R. D. Meade, and J. D. Joannopoulos, Phys. Rev. Lett. **61**, 1973 (1988).
[46]D. M. Kolb, G. Lehmpfuhl, and M. S. Zei, J. Electroanal. Chem. **179**, 289 (1984).
[47]A. J. Bard and L. R. Faulkner, *Electrochemical Methods* (Wiley, New York, 1980).
[48]A. Hamelin and J. P. Bellier, J. Electroanal. Chem. **41**, 179 (1973).
[49]A. Hamelin, J. Electroanal. Chem. **144**, 365 (1983).
[50]J. Lecoeur and A. Hamelin, C. R. Acad. Sci. Ser. C **279**, 1081 (1974).
[51]A. Hamelin and L. Stoicoviciu, J. Electroanal. Chem. **234**, 93 (1987).
[52]C. L. Fu and K. M. Ho, Phys. Rev. Lett. **63**, 1617 (1989).
[53]C. N. Chan, S. L. Cunningham, K. L. Luke, W. H. Weinberg, and S. P. Witherow, Surf. Sci. **78**, 15 (1978).
[54]B. E. Hayden, K. C. Prince, P. J. Davie, G. Paolucci, and A. M. Bradshaw, Solid State Commun. **48**, 325 (1983).
[55]V. Heine and L. D. Marks, Surf. Sci. **165**, 65 (1986).
[56]R. Smoluchowski, Phys. Rev. **60**, 661 (1941).
[57]D. M. Kolb and J. Schneider, Surf. Sci. **162**, 764 (1985).
[58]F. Sette, T. Hashizume, F. Comin, A. A. MacDowell, and P. H. Citrin, Phys. Rev. Lett. **61**, 1384 (1988).
[59]The decay time to the (1×1) state does not depend on the specifics of the grooming process.
[60]J. Wiechers, T. Twomey, D. M. Kolb, and B. J. Behm, J. Electroanal. Chem. **248**, 451 (1988).
[61]C. Alonso, R. C. Salvarezza, J. M. Vara, and A. J. Arvia, Electrochim. Acta. **35**, 1331 (1990).
[62]In the present measurements the intensity has been normalized in the wings of the Bragg peaks.
[63]In these measurements, the effective reflectivity is obtained by subtracting the diffuse background and normalizing to the absolute reflectivity at a fixed potential. This procedure assumes that the transverse line shape does not depend on potential.
[64]S. P. Witherow, T. H. Barret, and R. J. Culbertson, Surf. Sci. **161**, 584 (1985).
[65]D. M. Kolb, D. L. Rath, R. Wille, and W. N. Hansen, Ber. Bunsenges. Phys. Chem. **87**, 1108 (1983).